Journal of the Optical Society of America B
OPTICAL PHYSICS

Controlling the Gouy phase of coherent beams by necklace-like structures of optical vortices

N. Gorunski,[1] G. Maleshkov,[2] A. Stefanov,[2,3] M. Mincheva,[1] E. Lazarov,[1] I. Stefanov,[1] L. I. Stoyanov,[1,4,*] and A. Dreischuh[1,4,5]

[1]Department of Quantum Electronics, Faculty of Physics, Sofia University "St. Kliment Ohridski", Sofia, Bulgaria
[2]Department of Mechatronics, Robotics and Mechanics, Faculty of Mathematics and Informatics, Sofia University "St. Kliment Ohridski", Sofia, Bulgaria
[3]Institute of Mathematics and Informatics, Bulgarian Academy of Sciences, Sofia, Bulgaria
[4]National Centre of Excellence Mechatronics and Clean Technologies, Sofia, Bulgaria
[5]Bulgarian Academy of Sciences, Sofia, Bulgaria
*l.stoyanov@phys.uni-sofia.bg

Received 3 February 2026; revised 10 May 2026; accepted 20 May 2026; posted 20 May 2026; published 10 June 2026

Beyond its importance in physical optics, the Gouy phase also plays a crucial role in highly nonlinear processes such as above-threshold ionization and high-harmonic generation, owing to its scaling with the order of the nonlinear interaction. In this work, first, we show that the Gouy phase of coaxial superpositions of Laguerre–Gaussian vortex beams and Gaussian beams is always equal to the Gouy phase of an unperturbed Gaussian beam. Next, we numerically and experimentally demonstrate that the Gouy phase of a nearly Gaussian beam can be controlled when it carries a necklace-like structure of single-charge optical vortices in its wings. For this approach to work, it is essential for the vortices to be generated by pure phase modulation, which subsequently leads to their expected amplitude/intensity modulation. The presented numerical and experimental results indicate that the control of the Gouy phase is most effective when the number of vortices in the necklace-like structure is constant and its radius changes.

https://doi.org/10.1364/JOSAB.592638

1. INTRODUCTION

The Gouy phase is related to the axial phase shift experienced by any focused light beam passing through its focus with respect to a reference plane wave [1]. Without any claim for completeness, the early studies are related to the development of microwave optics [2], later to lasers [3], nonlinear optics [4], terahertz optics [5], and singular optics of phase [6] and polarization vortices [7], as well as quasi-non-diffracting beams [8]. The Gouy phase for a Gaussian beam is $\Phi_G = \arctan(z/L_D)$, where L_D is the Rayleigh diffraction length and z is the propagation coordinate. For a higher-order Hermite–Gaussian mode with mode indices (n, m), this phase is multiplied by a factor of $(1 + m + n)$ [9,10]. For a higher-order Laguerre–Gaussian modes with mode indices (l, p), the multiplication factor is $(1 + |l| + 2p)$ [11,12]. Here, $|l|$ accounts for the fact that the azimuthal mode index l is actually the topological charge (TC) of the on-axis point-phase dislocation, which can be both positive and negative. This point phase dislocation and the dark beam associated with it are known as an optical vortex (OV).

Optical vortices have spiral phase wavefronts and characteristic toroidal (doughnut-shaped) intensity profiles [13–15]. We stick in this work to canonical vortices, for which the spiral phase varies linearly with the azimuthal angle φ. The aforementioned TC corresponds to the total phase change $2\pi l$ over the azimuthal coordinate φ. Its sign depends on the sign of the azimuthal phase gradient [16]. In the context of this paper, it is worth mentioning that the dominant interaction between OVs with TCs of the same signs (nested on a common background) is the mutual repulsion and rotation of the OV pair with respect to the background beam axis [17]. However, in general, the interaction between OVs is much richer [15]. For some recent developments in the generation and application of structured light with OVs, please see also [18,19].

The Gouy phase plays an important role in both linear and nonlinear optics. The mode converter consisting of two cylindrical lenses is able to transform Hermite–Gaussian to Laguerre–Gaussian modes and vice versa [20]. Its operation is based on the dexterous use of the Gouy phase. In [8], it is shown both analytically and experimentally that the Gouy phase of long-range Bessel–Gaussian beams (BGBs) evolves nearly linear. For the same ring-shaped beam to be Fourier-transformed by a lens and for the same propagation distance of up to tens of centimeters, stronger focusing causes a larger Gouy phase shift of the BGB. This result confirms some earlier findings [6,21] showing that for strong focusing, the Gouy phase of BGBs

changes linearly for propagation distances of fractions of a millimeter.

The motivation behind this study is not only the importance of the Gouy phase in physical optics but also its application in nonlinear optics, where the phase scales with the order of the nonlinear process. For example, the efficiency of third-harmonic generation can be optimized by introducing a linear wave vector mismatch for compensating the Gouy phase shift [22]. Conversion between Laguerre–Gaussian modes in a four-wave mixing process is also observed and explained by the influence of the Gouy phase [23]. The Gouy phase has a strong influence on both processes involving phase synchronization and highly nonlinear processes like above-threshold ionization [24] and high-harmonic generation [25]. As following from its definition, the Gouy phase creates a longitudinal phase gradient that contributes to, e.g., the overall wavevector mismatch in the HHG process. Optimizing the position of the focus relative to the gas jet allows to partially cancel other phase-mismatch terms. The increase of the focal length of the used focusing lens results in a longer beam waist, i.e., a reduced Gouy phase gradient. The Gouy phase cannot be ignored, but it can be balanced with other phase components originating from the presence of neutral atoms, free (plasma) electrons, or nonlinear (dipole) refractive index changes. It seems that it would be beneficial to have a method for optimizing phase synchronization that does not require readjusting optical components and/or changing the intensity of the pump pulses.

The Gouy phase, Φ_G, is not an independent degree of freedom, as it depends on both the spatial distribution and the focusing geometry of the electromagnetic field. One approach to controlling the Φ_G is to adjust the focusing conditions—e.g., by varying the lens position or focal length, thereby modifying the beam waist size and location. Alternatively, the Gouy phase can be controlled independently along orthogonal directions using, for instance, cylindrical lenses, or by shifting the interaction region relative to the focus (or vice versa). Different laser modes accumulate distinct Gouy phase shifts; in general, their superpositions can therefore be used to tailor Φ_G as well. The novel results presented here can be regarded as an extension of this second general approach.

We confirm analytically and by numerical simulations what has been shown by Kovalev and co-workers in [26]—coaxial superpositions of Laguerre–Gaussian vortex beams and Gaussian beams have Gouy phases equal to the Gouy phase of an unperturbed Gaussian beam. Moreover, we demonstrate, for the first time to our best knowledge, that the Gouy phase of a nearly Gaussian beam can be controlled when it carries a necklace-like structure of single-charge OVs in its wings. By the rather vague term "nearly Gaussian," we mean a beam with a well-defined central peak (clearly dominating in the amplitude/intensity profile) and a bell-shaped transverse profile. This is still qualitative; however, operational classification excludes the Laguerre–Gaussian beams LG_p^l with topological charges $l \neq 0$ and/or radial index $p \geq 1$, as well as the Hermite–Gaussian beams, except the fundamental Gaussian HG_{00} mode and low-order super-Gaussian modes. For the purpose of the mentioned phase control, it is necessary for the OVs to be generated by pure phase modulation, which subsequently leads to their amplitude/intensity modulation. This approach allows us to reduce the rate of change of the Gouy phase Φ_G after the focus of the lens, with a general tendency to reach the asymptotic value of Φ_G for a Gaussian beam at larger beam propagation distances.

2. NUMERICAL APPROACH AND TEST RESULTS

A natural first step in this analysis is to calculate the Gouy phase of a Gaussian beam in the absence of OVs (setting the TC to $l = 0$) solving numerically the linear paraxial wave equation for the slowly varying optical beam envelope amplitude E:

$$i\partial E/\partial z + [1/(2k)](\partial^2/\partial_x^2 + \partial^2/\partial_y^2)E = 0, \quad \textbf{(1)}$$

where (x, y) are the Cartesian coordinates, ω_0 is the width of the Gaussian beam, k is the wavenumber, and $L_D = k\omega_0^2/2$ is the Rayleigh diffraction length. In order to calibrate the simulations, we modeled the focusing of a Gaussian beam with an initial beam width $\omega_0 = 5$ arb. units. Information on the longitudinal behavior of the peak intensity and the Gouy phase of this beam (on which the rings of vortices will be later formed) was extracted. The data are shown in Fig. 1. At the focus, the intensity of the beam increases 57.54 times to one arbitrary unit, which corresponds to a 7.6 times radial shrinking of the beam. Insofar as the simulation proceeds in numbers of computational steps from the beginning, the spherical phase distribution used to simulate the action of the focusing lens had its focus at the 175th step. The longitudinal coordinate z will be expressed in units of Rayleigh diffraction lengths z_R for the Gaussian beam that is universally used as a background beam and will be denoted as z/z_R. From the Gouy phase in the calibration simulation (Fig. 1), using the theoretical relation $\Phi_G = \arctan(z/z_R)$ [1], we obtained that $z_R = 22$ computational steps. Returning to the position of the focusing lens, we can now note that it is positioned $0.5z_R$ after the beginning of each simulation and $-7.5z_R$ from the focus of the unperturbed background Gaussian beam.

The reported numerical simulations of necklace-like structures of optical vortices are based on Eq. (19) in [26], describing coaxial superpositions of Laguerre–Gaussian (LG) vortex beams and Gaussian beams:

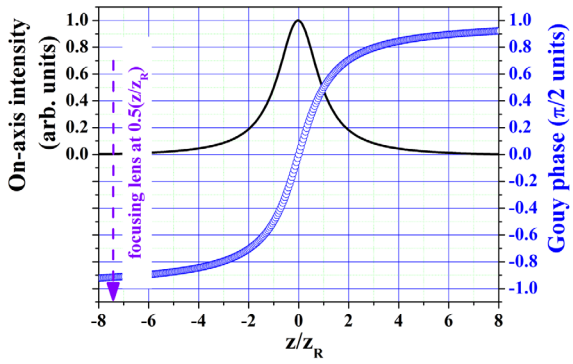

Fig. 1. Left scale: On-axis intensity (solid curve) of an unperturbed Gaussian beam freely propagating from the beginning of the simulation at -8 Rayleigh diffraction lengths (z_R) to the plane of the simulated thin focusing lens placed at $-7.5(z/z_R)$ and further to its focus (at $z = 0$) and to $+8(z/z_R)$. Right scale: Accumulated Gouy phase (hollow circles) in the course of the described propagation of the Gaussian beam, presented in $\pi/2$ units.

$$E(r,\varphi,z)=\frac{1}{q}\exp\left(-\frac{r^2}{q\omega_0^2}\right)\left(\frac{r^m e^{im\varphi}}{q^m}-r_0^m\right), \quad (2)$$

where

$$q=\sqrt{1+(z/L_D)^2}e^{i\Phi_G}, \quad (3)$$

$$\Phi_G=\arctan(z/L_D). \quad (4)$$

Here, (r,φ) are the polar coordinates related to the Cartesian coordinates (x,y), whereas m is the number of optical vortices with unit topological charge ($|l|=1$) located like a necklace along an imaginary circle of radius r_0 in the wings of the Gaussian host beam. In the above relations, $L_D=k\omega_0^2/2$ is the Rayleigh diffraction length, ω_0 is the Gaussian beam waist radius, and k is the wavenumber in the medium, respectively. It follows from Eqs. (2)–(4) that the real and imaginary parts of the initial (here at $z=0$) amplitude ($E(r,\varphi,z=0)$) and the phase profiles ($\Phi(r,\varphi,z=0)$) of the coaxial superpositions of LG vortex beams and a Gaussian beam are

$$\mathrm{Re}[E(r,\varphi,z=0)]=\exp\left(-\frac{r^2}{\omega_0^2}\right)[r^m\cos(m\varphi)-r_0^m], \quad (5a)$$

$$\mathrm{Im}[E(r,\varphi,z=0)]=\exp\left(-\frac{r^2}{\omega_0^2}\right)r^m\sin(m\varphi), \quad (5b)$$

$$\Phi(r,\varphi,z=0)=\arctan\left(\frac{\mathrm{Im}[E(r,\varphi,z=0)]}{\mathrm{Re}[E(r,\varphi,z=0)]}\right)=\arctan\left(\frac{r^m\sin(m\varphi)}{r^m\cos(m\varphi)-r_0^m}\right). \quad (5c)$$

To allow the reader to get a clearer picture of the beams described by Eqs. (5), in Fig. 2, we show the initial transverse distributions of the real ($\mathrm{Re}[E]$) and imaginary ($\mathrm{Im}[E]$) parts of the electric field E, as well as the intensity ($I=\mathrm{Re}^2[E]+\mathrm{Im}^2[E]$) and phase distributions $\Phi(r,\varphi)$ [see Eq. (5c)] of the necklace-like vortex beams for $m=3$, 6, and 9 optical vortices. The normalized beam intensities are presented in grayscale. The same is done for the phase distributions, with black and white corresponding to phases zero and 2π. In this sense, the black-to-white transition lines that extend from the centers of the panels to their peripheries do not denote phase jumps. The centers of the vortices are in the positions around which (along circular trajectories) the phases change from black to white, i.e., from 0 to 2π. The same phase gradients are indicative of the fact that all OVs have the same sign of their unit TCs. In the rightmost column of panels, we show phase portraits of the same vortex-necklace beams generated by replacing the term $(-r_0^m)$ in Eq. (5c) by $(+r_0^m)$. This was done intentionally to show the potential advantage of this substitution in avoiding unnecessary $(0-2\pi)$ transitions which, in the case of an, e.g., imperfect calibration of the used phase modulators, could lead to noisier experimental data. Numerical simulations proved that such a sign change does not result in a change of the longitudinal behavior of the Gouy phase. However, in this work, we continued to use the original result given by Eq. (5c).

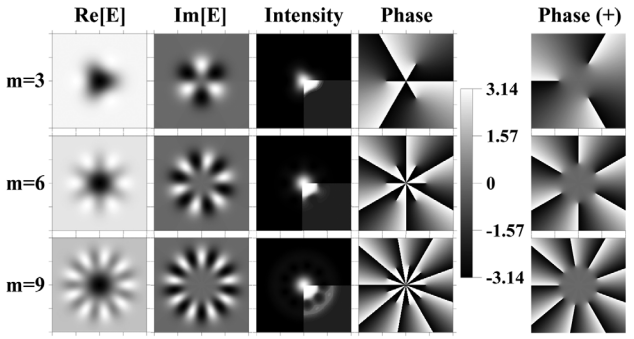

Fig. 2. Transverse distributions of the real ($\mathrm{Re}[E]$) and the imaginary part ($\mathrm{Im}[E]$) of the electric field E, as well as intensity ($I=\mathrm{Re}[E]^2+\mathrm{Im}[E]^2$) and phase portraits ($\Phi=\arctan(\mathrm{Im}[E]/\mathrm{Re}[E])$) of the beams described by Eqs. (5a)–(5c) for $m=3$, 6, and 9 OV. For this figure only, the computational windows span over $[-1,+1]\times[-1,+1]$ arb. units, $\omega_0=0.28$ arb. units and vortex ring radius $r_0=1.5\omega_0$. For better visibility of the OVs in the wings of the host beams, one quarter of each intensity distribution is additionally adjusted in brightness and contrast. Rightmost column of panels—phase portraits of the same vortex-necklace beams generated by replacing $(-r_0^m)$ by $(+r_0^m)$ in Eq. (5c). See the text for details.

Each simulation presented here ran in a computational window spanning over 1024×1024 points discretizing the interval from -25 to $+25$ arbitrary units. The radius of the background Gaussian beam (at $1/e^2$ intensity level) is always kept $\omega_0=5$ arb. units. An appropriate change in the spherical phase distribution used to simulate the action of the focusing lens results in the simulated action of a lens with a different focal length. Stronger focusing of the beam would lead to its stronger expansion behind the focal plane. The corresponding simulation of the beam's behavior, without numerical errors occurring at the edges of the computational window, would require doubling (or quadrupling) the size of the computational grid (e.g., to 2048×2048 points). Due to the expected shorter Rayleigh diffraction length, we would also expect higher gradients of the Gouy phase Φ_G around the focus. Qualitatively, we would expect the influence of the necklace-like structure on Φ_G to be the same.

An important, albeit negative, result in the context of this work is the following: With simultaneous initial amplitude and phase modulation corresponding to Eq. (5), the Gouy phase behavior of this complex superposition of beams is always the same as that of the undisturbed host Gaussian beam. The analytical proof of this statement can be found in Appendix A. Here, we prefer to present the results of numerical simulations supporting this statement.

In Fig. 3, we show numerical results on the evolution of coaxial superpositions of Laguerre–Gaussian vortex beams and a Gaussian beam [26] [beams described by Eqs. (5a)–(5c)] for normalized vortex necklace-ring radius $r_0/\omega_0=1.3$ and for $m=3$, 6, 9, and 12 OVs. The initial amplitude, phase, and intensity distributions of such superpositions are intentionally chosen to correspond to substantially different diametral distributions of the beam intensities. They range from a nearly Gaussian distribution ($m=3$) and one with a clearly dominant central peak ($m=6$), to a distribution with three transverse

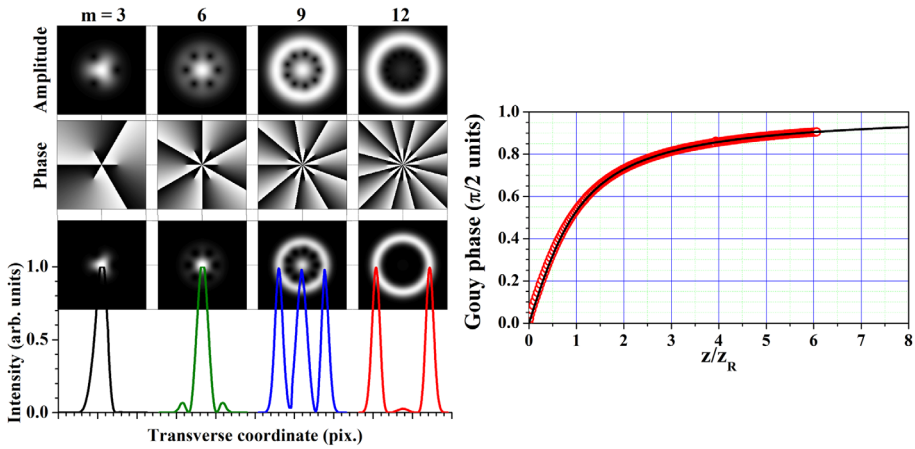

Fig. 3. Left set of panels: Initial amplitude (upper row), phase (middle), and intensity distributions (lower row and graphs below) and transverse cross-sections of the beams described by Eqs. (5a)–(5c) for $r_0/\omega_0 = 1.3$ and $m = 3$, 6, 9, and 12 OVs, for which the Gouy phase (right graph) is calculated (red open circles) up to propagation distances of six Rayleigh diffraction lengths. Black solid curve—the theoretical Gouy phase of the unperturbed Gaussian beam.

peaks ($m = 9$) and as well as to one with two more distant dominant transverse peaks ($m = 12$). All results shown in Fig. 3 are in agreement with the analytical result in A, proving that the Gouy phase Φ_G for coaxial superpositions of a LG vortex beam and a Gaussian beam has the behavior of Φ_G for an unperturbed Gaussian beam. As seen in the graph in Fig. 3, in all these cases, the calculated Gouy phase evolves from the beam waist to "infinity" following the dependence $\Phi_G = \arctan(z/L_D)$ and tending asymptotically to $\pi/2$. The only difference arising from the width of the used computational window was that for 9 and 12 OVs, the simulations were terminated at $5z_R$ and $4z_R$, respectively, due to indications of the onset of accumulation of computational error. The reader may wish to focus on the panels corresponding to $m = 3$ and 6 OVs. With the specific choice of $r_0/\omega_0 = 1.3$, the aforementioned situation of a dominating single central peak is realized.

By fixing the number of OVs arranged in a necklace-like structure to $m = 3$, we also calculated the corresponding Gouy phases for coaxial superpositions of Laguerre–Gaussian vortex beams and a Gaussian beam for ratios $r_0/\omega_0 = 0.9$, 1.1, 1.3, and 1.5. For all these substantially different beams, it was numerically confirmed that starting from the beam waist to "infinity," the Gouy phase evolves according to the dependence $\Phi_G = \arctan(z/L_D)$, characteristic for the Gaussian beam. To avoid overloading the paper, examples of such beams are shown in Fig. 11 in Appendix B, while other simulated cases (for $m = 6$ and 9) are completely omitted.

To preclude the impression that the software consistently produces identical outcomes, we numerically modeled the evolution of the Gouy phase for Laguerre–Gaussian beams with azimuthal mode indices $|l| = 0$, 1, 3, 6, and 9 and with a radial mode index $p = 0$ starting from the beam's waist. In terms of Eq. (5), the radius r_0 of the imaginary vortex necklace was set equal to zero. Graphically, the obtained results are shown in Fig. 12 in Appendix B. They are perfectly consistent with the analytical relation stating that for higher-order Laguerre–Gaussian modes, the Gouy phase of the Gaussian beam $\Phi_G = \arctan(z/L_D)$ is multiplied by a factor of $(1 + |m| + 2p)$, where in our analysis $|m| = l$ and $p = 0$ [11,12].

The goal of this work is to find an approach for controlling the Gouy phase of coherent laser beams by necklace-like structures of optical vortices. In view of this, the above results seem negative. As we will show later, it is essential to initially modulate the phase of the host Gaussian beam only. In its originally flat phase profile, one has to imprint the phase of a ring-like (necklace-like) structure of optical vortices with unit topological charges of equal signs, as analytically described by Eq. (5c). Of course, the phase modulation gives rise to an amplitude modulation. Under amplitude modulation generated by initial pure phase modulation, the Gouy phase Φ_G evolves in a different way. Furthermore, the focus of this analysis is placed on the possibility to control the longitudinal rate of change of Φ_G.

3. EXPERIMENTAL SETUP AND SIGNAL PROCESSING

In order to experimentally record Gouy-phase-dependent interference signals from the beams carrying necklace-like structures of OVs, we used a single-lens interferometer [27,28] consisting of a focusing lens with no antireflection coatings only [see part (a) of Fig. 4]. After two Fresnel reflections from its surfaces (see points marked with 1 and 2), a strongly converging secondary ("ghost") beam is formed. This reflected beam is coaxial with respect to the main "background" beam. Its secondary focal plane is much closer to the lens than its usual focal plane. According to [28], the distance f_{eff} from the lens to the "ghost" beam waist is related to the focal length f of the lens by $f_{eff} = f(n-1)/(3n-1)$, where n is the refractive index of the lens' glass. Despite its significantly lower intensity relative to the background beam, the secondarily reflected beam reaches sufficient intensity in its focal region to provide an excellent modulation depth of the interference pattern with the slightly converging background beam. The range of existence of this pattern is, however, of the order of only a few centimeters, depending on the focal length of the lens L.

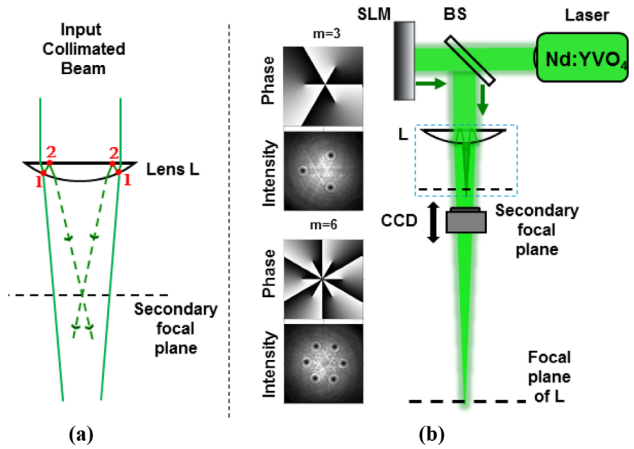

Fig. 4. Sketch of the principle of operation of the single-lens interferometer (SLI) (a) and SLI aligned in the used experimental setup (b). Laser—continuous-wave Nd : YVO_4 laser with intracavity second-harmonic generation emitting at 532 nm. BS—beam splitter. SLM—liquid crystal spatial phase modulator. L—uncoated focusing lens ($f = 150$ cm). CCD—charge-coupled device camera mounted on a translation stage. Dashed rectangle—single-lens interferometer. Frames to the left—numerically generated phase and power density profiles of beams carrying necklace-like structures with $m = 3$ and $m = 6$ OVs.

Figure 4(b) shows the used experimental setup. The beam from a continuous-wave Nd : YVO_4 laser with intracavity second-harmonic generation ($\lambda = 532$ nm) illuminates the reflective liquid crystal spatial phase modulator SLM (HoloEye; model PLUTO, 1920 pix. × 1080 pix. with a pixel pitch of 8.8 μm), programmed with the desired phase distribution. The phase-modulated beam, in which amplitude/intensity modulation also develops, is (partially) reflected by the beam splitter BS and passes through the single-lens interferometer [an uncoated focusing lens L ($f = 150$ cm)]. A charge-coupled device camera (CCD) mounted on a translation stage is used to record the interference patterns around the beam waist of the "ghost" beam. The frames to the left show two examples of numerically generated phases sent to the SLM and calculated power density profiles of beams carrying necklace-like structures with $m = 3$ and $m = 6$ OVs, as expected to be observed in front of the lens L.

Figure 5(a) shows an example of the modulated background beam with 6 OVs ($r_0/\omega_0 = 0.8$) formed on it and captured in the near field just before the lens L. Frames (b1)–(b3) show the recorded interference signals in the secondary focal plane [frame (b2)] and at two symmetrical positions before [frame (b1)] and after it [frame (b3)]. For better visibility, frames (b1)–(b3) are magnified by a factor of 5. The change in the overall curvature of the wavefront before and after the secondary focal plane is the reason why the six interference spirals twist in opposite directions, becoming nearly radial in the vicinity of this plane.

As discussed, the CCD camera was moved along the beam axis around the secondary focal plane. At each position, it captured an interferogram similar to those shown in Figs. 5(b1)–5(b3). From each such interferogram, we evaluated the intensity at the center of the interference pattern. The set of data obtained in this way will be denoted as an axial interference signal. One such signal, normalized to the interval [0,1], is shown in the left graph in Fig. 6. An important first step in processing the experimental data is to construct a fit function that adequately describes the recorded interference signal $I(z)$ along the propagation coordinate z. In terms of the intensities of the individual waves, it can be expressed as

$$I(z) = I_R(z) + I_{ghost}(z) + \sqrt{I_R(z) I_{ghost}(z)}\cos[\varphi_R(z) - \varphi_{ghost}(z) + \varphi_0], \quad \textbf{(6)}$$

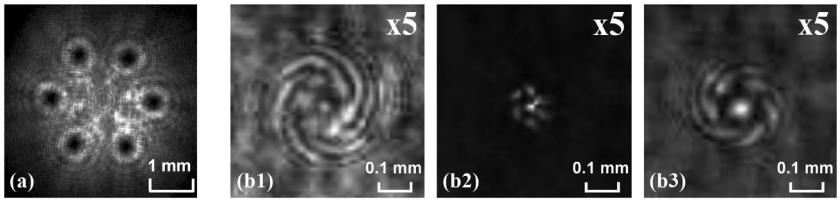

Fig. 5. Experimental data. Modulated Gaussian beam carrying a necklace-like structure of OVs with units TCs after its reflection from the SLM (a) and patterns recorded in the single-lens-interferometer in front of (b1), at (b2), and behind the secondary focal plane (b3). Frames (b1)–(b3) are magnified by a factor of 5.

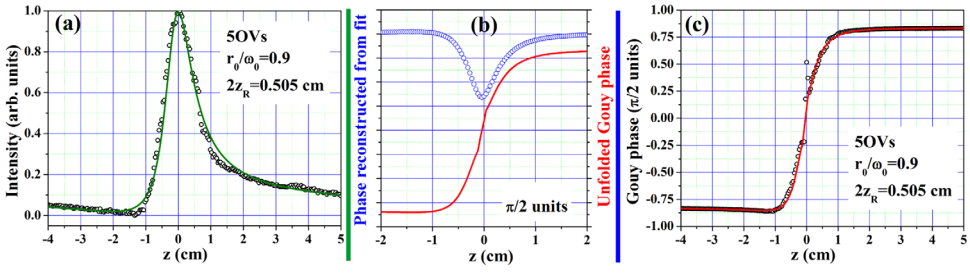

Fig. 6. Procedure for extracting the Gouy phase from the experimental data for a necklace-like structure of 5 OVs and $r_0/\omega_0 = 0.9$. (a) Normalized interference signal (hollow circles) and approximating function $f(z)$ (green solid curve) according to step (a1) described above. (b) Phase, reconstructed from the fit $f(z)$ [hollow blue circles; step (b)] and unfolded Gouy phase [red solid curve; step (c)]. Graph (c) Unfolded Gouy phase from the fit $f(z)$ [red solid curve; step (c)] and Gouy phase retrieved from the experimental data [black hollow circles; step (d)].

where I_R is the intensity of the reference beam and I_{ghost} is the intensity of the secondary ("ghost") beam. In the "ghost" beam focal region, the intensity of the secondary beam varies strongly depending on the "ghost" beam width $\omega(z)$ and can be approximated by $I_{ghost}(z) = I_{ghost}(z=0)/\omega(z)$. Here, we assume a Gaussian background beam shape, $\omega(z) = \omega(z=0)\sqrt{(1+(z/L_D)^2)}$, where L_D is the Rayleigh diffraction length. It is worth noting that in the interference term, this intensity appears in the square root function. In contrast, in this range (around the secondary focal plane), the background (reference) beam converges only slightly. The weak change in its intensity could be neglected in the square root function and can be approximated by a linear function in the first summand. It can be further assumed that, within the range of propagation lengths in which the measurement is performed, its phase does not change significantly as well (i.e., $\varphi_R(z) = const$). The phase $\varphi_{ghost}(z)$ of the secondary focused beam is, however, of particular importance. Since the processed interference signal is measured along the beam propagation axis, the Gouy phase Φ_G should be involved here, through a dependence of the type $\arctan(z/L_D)$. The function approximating the interference signal should also include parameters that account for a possible slight shift of the secondary focus from the secondary focal plane and for a possible constant phase shift φ_0.

To extract the Gouy phase from the experimental data, we applied the following sequence of operations:

/a1/ Approximate the normalized interference signal with a function of the type $f(z) = A + B(z-C) + D/\sqrt{1+(z+E)^2/F^2}\cos[\arctan((z+E)/F) + H]$, where z is the longitudinal coordinate and $F = z_R$ is the Rayleigh diffraction length. The term $A + B(z-C)$ accounts for the slow change of the main beam, experiencing the usual focusing by the lens L of a focal length f. D is a normalization constant. The denominator $\sqrt{1+(z+E)^2/F^2}$ accounts for the variable intensity of the "ghost" beam around the secondary focus. E reflects a possible weak shift of the secondary focus from the secondary focal plane, and H is a constant phase shift;

/a2/ For shorter notation, let us formally introduce the functions $g(z) = A + B(z-C)$ and $h(z) = D/\sqrt{1+(z+E)^2/F^2}$;

/b/ Calculate the phase reconstructed from the fit $f(z)$ using $\arccos[f(z) - g(z)]/h(z)$;

/c/ Unfold the obtained approximation phase, shift it (if necessary) and present it in the $[-\pi/2, +\pi/2]$ interval;

/d/ Apply $\arccos(\ldots)$ to the experimental data and repeat the procedure in point **/c/**.

The described sequence of operations applied to a necklace-like structure composed of 5 optical vortices, with a ratio of the radius of the vortex ring to the radius of the background beam of $r_0/\omega_0 = 0.9$, is visualized in Fig. 6.

The single-lens interferometer is a simple device that is easy to adjust and use. Unfortunately, for quantitative measurements such as those reported here, it has some drawbacks. First, the focusing lens used must not be too short-focus, so that the secondary focal plane is not too close to the lens. On the one hand, this would make it difficult for the camera to follow the evolution of the beam before the secondary focus, and on the other hand, the beam would be focused too tightly. Moreover, the strong focusing would make it difficult to extract the interference signal and the Gouy phase precisely in the region in which the change of the quantities is the fastest. Another potential source of errors in relation to the strong focus is keeping the dynamic range settings of the CCD camera the same for the whole scan (before the secondary focal plane, in it, and after it).

As shown in Fig. 5, panel (b2), aberrations of the strongly focused (secondary) beam due to aberrations of the lens can arise, affecting the interaction between the optical vortices. As a result, the OV ring can be deformed, and thus, the peak can shift away from the beam's propagation axis. Another thing worth mentioning is that the narrow focal peak means that the interference pattern within it is not clearly visible and may be affected by the crosstalk between adjacent pixels of the CCD camera. All this sounds like a series of shortcomings of the single-lens interferometer, but these are compensated for by the device's stability with respect to fluctuations in the parameters of the used laser beam.

In our opinion, the main source of noise in the experimental data is the mechanical vibrations in the plane transverse to the beam propagation axis, along which the position of the CCD camera varies. In the experiments, the axial interference signal was extracted by integrating over a 2×2-pixel region (the same for all frames). Thus, the resolution of the extracted data is 9 μm. The extracted signals from the individual scans under comparable conditions were reproducible. In the data presented here, we did not average axial interference signals from successive measurements but each time used one of them.

4. RESULTS

Another thing worth commenting on is that the numerical simulations are consistent with the experimental conditions. In both cases, the number of optical vortices is varied from 2 to 6 by changing the pre-calculated phase distributions that are sent to the phase-only liquid crystal spatial light modulator (SLM). Before the SLM, the laser beam size ω_0 is not changed. The fine-tuning of the normalized vortex necklace-ring radius r_0/ω_0 is achieved by numerical resampling of the aforementioned phase distributions. To avoid potential edge effects from the periphery of the modulator, the phase distributions were calculated over a wider (than the HDMI standard) grid of points and were always downscaled to the desired value of r_0/ω_0.

A. Constant Necklace-Ring Radius r_0 and Variable Number of OVs

First, we would like to present results when the necklace-ring radius was kept constant, and we varied the number of OVs in the necklace-ring. In this case, keeping the ratio of the vortex ring radius to the background beam radius $r_0/\omega_0 = 0.6$, the general tendency observed in the numerical simulations is a monotonic decrease in the rate of change of the Gouy phase behind the beam foci, with increasing the number of OVs in the necklace structure (from 2 to 6). This is clearly expressed in the enlarged graphs on the right in Figs. 7(a) and 7(b). Each of these figures is composed of two panels—a smaller one, showing the numerical data from the beginning of the simulation to about

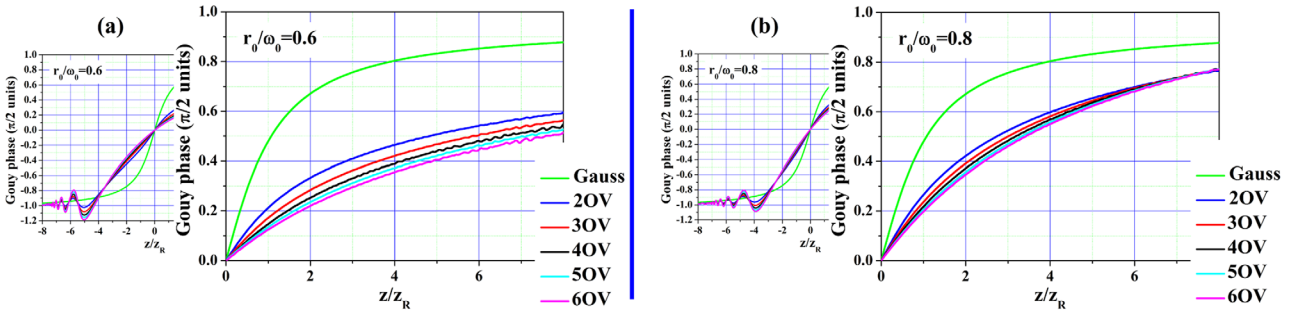

Fig. 7. Numerical results. Longitudinal evolution of the Gouy phase of a pure Gaussian beam and of necklace-rings with $r_0/\omega_0 = 0.6$ (a) and $r_0/\omega_0 = 0.8$ (b) for different numbers of OVs arranged in the structure. In all graphs, the same colors are used to denote the cases with the same numbers of OVs.

$1z_R$ behind the focus, and a larger one showing, in more detail, the evolution of the Gouy phase until the end of the simulation ($z = 8z_R$). In the small left panels in Figs. 7(a) and 7(b), transient oscillations are visible in the Gouy phase, which stabilize upon approaching the focus of the lens. The reason for the oscillations is that the Gaussian beam is modulated only in phase, which leads to the development and subsequent stabilization of amplitude modulation (see, for example, Fig. 3 in [29]). It can also be seen that when the OVs are closer to each other at the beginning [Fig. 7(a); $r_0/\omega_0 = 0.6$], the oscillations have higher amplitudes than in the case when the OVs are further apart at the beginning [Fig. 7(b); $r_0/\omega_0 = 0.8$]. It is worth noting that in our experimental data [see, for example, Fig. 6(a)], such oscillations were not registered. One possible explanation is that in a single-lens interferometer, an interference signal appears only within a narrow range of propagation distances, in which the intensity of the secondarily focused beam is comparable to that of the slowly converging background beam. Another probable reason is that the SLM-beam splitter-lens distance is 15 cm, and thus the oscillations have damped out.

Looking at the overlaid downscaled graphs in Figs. 7(a) and 7(b), increasing the number of OVs in the ring, the Gouy phase shows oscillatory behavior toward the focus. The small left panels in Figs. 7(a) and 7(b) [as well as those in Figs. 8(a) and 8(b)] use the same color coding for the different curves as those in the respective large panels to the right, indicating the different number of OVs. After the focus, at $r_0/\omega_0 = 0.6$ [Fig. 7(a), the enlarged graph], the Gouy phase monotonically decreases with increasing the number of OVs. At $r_0/\omega_0 = 0.8$ [Fig. 7(b), the enlarged graph], this is true only up to $z/z_R \sim 6$; then the curves intersect, and it appears that the tendency is reversing.

We use the same graph style to present the experimental data in Fig. 8. In the downscaled graphs in Figs. 8(a) and 8(b), before reaching the secondary focal plane (see Fig. 4), we present only the curves interpolating the experimental data. The absence of transient oscillations is clearly visible. The curves intersect only in the focal plane. The enlarged graphs to the right show the behavior of the reconstructed Gouy phase after the focus. The continuous curves represent the approximating functions, while the colored hollow circles represent the processed experimental data. It can be seen that the experimental data fit well with the theoretical prediction: as the number of optical vortices in the circular structure increases, the growth rate of the Gouy phase decreases with the offset from the focus. It is also well pronounced that the experimental data for $r_0/\omega_0 = 0.6$ [Fig. 8(a)] are much noisier near the focus than those for $r_0/\omega_0 = 0.8$ [Fig. 8(b)]. Repeating this and other similar measurements multiple times did not improve the results. We explain this by the fact that at $r_0/\omega_0 = 0.6$, the optical vortices are formed closer to each other and interact more strongly (by rotating around the axis of the beam and by mutual repulsion), and a certain propagation length is required before the trends in the Gouy phase evolution stabilize. At a larger initial distance between the vortices [$r_0/\omega_0 = 0.8$, Fig. 8(b)], their interaction should be weaker and, as a result, the experimental data deviate much

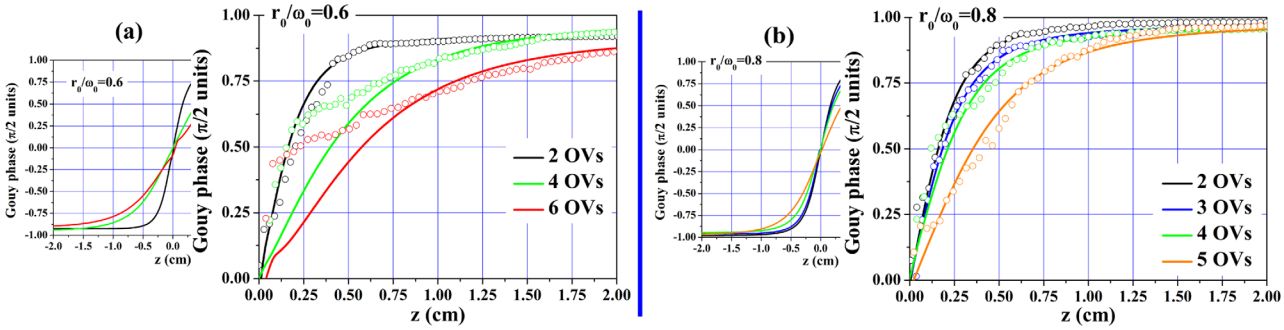

Fig. 8. Experimental data. (a) Longitudinal evolution of the Gouy phase of the necklace-rings presented by the analytical fits (solid curves) for $r_0/\omega_0 = 0.6$ and a variable number of OVs (2, 4, and 6). The magnified graph placed to right shows the processed experimental data (hollow circles) behind the secondary focus of the lens and the corresponding fits. (b) The same as in panel (a) for $r_0/\omega_0 = 0.8$ and for variable number of OVs (ranging from 2 to 5).

less from the approximating functions for the Gouy phase. In general, an additional recommendation is to use a lens L with a longer focal length, so that the focal spot at the secondary focus is larger, leading to weaker pixelation of the interference pattern and to reduced noise in the experimental data.

B. Constant Number of OVs and Variable Necklace-ring Radius r_0

In this second studied case, we keep the number of OVs constant [2 and 5 for Fig. 9(a) and 9(b), respectively] and use the same background beam width ω_0. Behind the beam foci, the general tendency deduced from the numerical simulations is a monotonic decrease in the rate of change of the Gouy phase with decreasing the necklace ring radius r_0. This key tendency is clearly visible in the enlarged front graphs in Figs. 9(a) and 9(b) (compare, e.g., the black, light blue, and red curves in each graph separately). The evolution of the Gouy phase from the beginning of the simulations is shown in the overlaid downscaled graphs in Figs. 9(a) and 9(b). Again, as in the previous case, oscillations are visible, which decay as they approach the focus, but with no crossing of the curves after the oscillations stabilize. It is also evident that the oscillations are stronger for necklace-rings containing a higher number of OVs, in this case—5 compared with 2. This is consistent with our hypothesis expressed in relation to the downscaled graphs in Figs. 7(a) and 7(b). Most likely, the oscillations are due to the fact that the Gaussian beam is modulated only in phase, which leads to the development of amplitude modulations, and these modulations are stronger the greater the number of optical vortices is.

Figure 10 shows the experimental data for necklace-like structures with different values of r_0/ω_0 for three different cases of 2, 4, and 5 OVs, respectively. Here, the Gouy phase extracted from the data is shown by hollow circles, with the curves represented by solid lines being data extracted from the approximation functions of the data. The least noisy data are those for 2 OVs, while those with 4 OVs are relatively the noisiest. Generally, at a qualitative level, the experimental results support the theoretical prediction that the rate of increase of the Gouy phase after the lens secondary focus decreases with decreasing the radius of the circle r_0 along which the vortices are arranged. In two of the cases, the behavior of the Gouy phase for an unperturbed Gaussian beam from the corresponding series of measurements is also shown. Unfortunately, no such curve is shown in the left graph of Fig. 10. The reason is that the obtained result does not match the trend that the Gouy phase for a Gaussian beam has the highest rate of increase along the propagation direction.

C. Discussion

In order to understand the observations regarding which of the two approaches are more efficient: variation of the radius of the vortex ring structure or increasing the number of OVs in the ring, one should remember the basic interactions between OVs. It has been demonstrated that a pair of singly and equally charged OVs placed on a bright background beam rotate and repel each other (see [3]), whereas OVs of opposite TCs translate with respect to the background beam, attract each other, and eventually annihilate. In all cases presented in this work, the vortex necklace structures are composed of singly charged OVs with equal TCs. This means that while propagating, the vortex

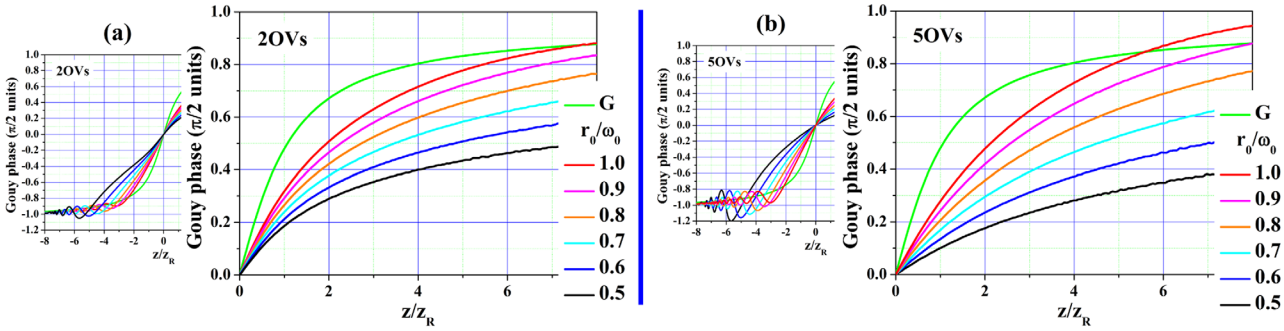

Fig. 9. Numerical results. Longitudinal evolution of the Gouy phase for a pure Gaussian beam and for different necklace ring radii-to-background beam radius r_0/ω_0 ranging from 0.5 to 1.0 [2 OVs (left) and 5 OVs (right)]. Across all graphs, identical colors are used to represent the same value of the ratio r_0/ω_0, facilitating comparison of corresponding cases between panels.

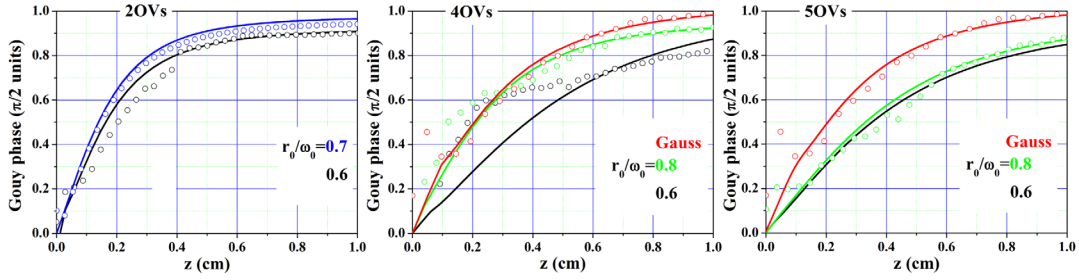

Fig. 10. Experimental data. Longitudinal evolution of the Gouy phase presented by the analytical fits to the obtained experimental data (solid curves) and data retrieved from the experiment (hollow circles) for different necklace ring radii-to-Gaussian beam width r_0/ω_0 in three different cases (2, 4, and 5 OVs).

ring structure rotates but also the individual OVs composing the structure are repelling each other.

In the context of this work, in our opinion, the repulsion between OVs with identical signs of their unit topological charges seems to be more important than the rotation of the necklace structure around the background beam axis. It is known that (see Fig. 1 in [30]) the repulsion of the OVs is inversely proportional to the distance between any two adjacent vortices. A simplified estimation shows that, on an imaginary circle of radius r_0, the distance between two adjacent vortices (out of the total N vortices) varies more significantly for a constant number of vortices N, with changing the radius of the necklace-like structure r_0, than for a constant radius r_0 with changing the number of vortices N. In other words, by keeping the number of OVs constant and varying the necklace-ring radius, one can more effectively control the Gouy as compared to the opposite case when the radius of the necklace-ring is kept constant and the number of OVs in the necklace-ring is changed.

5. CONCLUSION

In this work, we show both numerically and experimentally that the rate of change of the Gouy phase of a nearly Gaussian beam carrying a necklace-like structure of single-charged optical vortices can be effectively controlled by both the number of optical vortices in its wings and by the radius of the necklace structure. For this purpose, it is necessary for the vortices to be generated by pure phase modulation, which subsequently leads to their usual amplitude/intensity modulation. The presented results show that the control of the Gouy phase is most effective when the number of vortices in the necklace-like structure is constant, and its radius changes. Based on our experience with this problem so far, practical limits are normalized vortex necklace-ring radius $r_0/\omega_0 = 0.5$ and higher, as well as less than 10 optical vortices in the necklace-like ring formation. At this stage, we are not yet able to determine whether the observed changes in the Gouy phase slope (see, e.g., Figs. 7–10) are sufficiently large to be of practical relevance. In this regard, we understand that some readers may view the reported results primarily as a proof-of-principle rather than as a method ready for immediate application. Nevertheless, we believe that these findings provide a valuable basis for future numerical simulations and experimental investigations.

APPENDIX A

1. Circular Array of Optical Vortices

As mentioned, a necklace-like structure of optical vortices can be considered as a superposition of Laguerre–Gaussian (LG) and pure Gaussian modes [26], i.e.,

$$E(r,\varphi,z) = \frac{e^{izk}}{q(z)} \exp\left(-\frac{r^2}{q(z)\omega_0^2}\right)\left(\frac{r^m e^{im\varphi}}{q(z)^m} - r_0^m\right), \tag{A1}$$

where

$$q(z) = 1 + i\frac{z}{z_0} = \frac{z_0 + iz}{z_0}, \tag{A2}$$

and z_0 stands for the Rayleigh diffraction length L_D. Note that in [26] the e^{izk} term is omitted. The term in the exponent can be rewritten as

$$\frac{r^2}{q(z)\omega_0^2} = \frac{r^2 z_0}{z_0 + iz}\frac{1}{\omega_0^2} = \frac{r^2 z_0}{\omega_0^2}\frac{z_0 - iz}{z_0^2 + z^2}. \tag{A3}$$

Then

$$\begin{aligned}\frac{1}{q(z)} &= \frac{z_0}{z_0 + iz} = \frac{z_0}{z_0^2 + z^2}(z_0 - iz)\\ &= \frac{z_0}{z_0^2 + z^2}\sqrt{z_0^2 + z^2}\exp\left(-i\operatorname{atan}\frac{z}{z_0}\right)\\ &= \frac{z_0}{\sqrt{z_0^2 + z^2}}\exp\left(-i\Phi(z)\right), \quad \Phi(z) = \operatorname{atan}\frac{z}{z_0}.\end{aligned} \tag{A4}$$

In this way, the electric field amplitude of the necklace-like structure of optical vortices becomes

$$\begin{aligned}E(r,\varphi,z) = \frac{e^{izk}z_0}{\sqrt{z_0^2 + z^2}} e^{-i\Phi(z)} \exp\left(-\frac{r^2 z_0^2}{\omega_0^2(z_0^2 + z^2)}\right)\\ \times \exp\left(i\frac{r^2 z z_0}{z_0^2 + z^2}\right)\left(\frac{r^m z_0^m}{\sqrt{z_0^2 + z^2}^m} e^{im(\varphi - \Phi(z))} - r_0^m\right).\end{aligned} \tag{A5}$$

2. Analysis of the Gouy Phase

For any complex-valued function $f(z) = |f|e^{i\phi}$, the phase ϕ can be found by

$$\phi = -i\operatorname{Log}\left(\frac{f(z)}{|f(z)|}\right), \tag{A6}$$

where Log denotes the principal value since complex logarithms are multi-valued.

From Eq. (A5), it follows that

$$\begin{aligned}|E(r,\varphi,z)| &= \sqrt{E(r,\varphi,z)E^*(r,\varphi,z)}\\ &= \frac{z_0}{\sqrt{z_0^2 + z^2}} \exp\left(-\frac{r^2 z_0^2}{\omega_0^2(z_0^2 + z^2)}\right)\\ &\times \sqrt{\frac{(z_0 r)^{2m}}{\sqrt{z_0^2 + z^2}^{2m}} - 2\frac{(r r_0 z_0)^m}{\sqrt{z_0^2 + z^2}^m}\cos\left(m(\varphi - \Phi(z))\right) + r_0^{2m}}.\end{aligned} \tag{A7}$$

Thus, we get

$$\begin{aligned}F(r,\varphi,z) = \frac{E(r,\varphi,z)}{|E(r,\varphi,z)|} = e^{izk}e^{-i\Phi(z)}\exp\left(i\frac{r^2 z z_0}{z_0^2 + z^2}\right)\\ \times \frac{\left(\frac{r^m z_0^m}{\sqrt{z_0^2 + z^2}^m} e^{im(\varphi - \Phi(z))} - r_0^m\right)}{\sqrt{\frac{(z_0 r)^{2m}}{\sqrt{z_0^2 + z^2}^{2m}} - 2\frac{(r r_0 z_0)^m}{\sqrt{z_0^2 + z^2}^m}\cos\left(m(\varphi - \Phi(z))\right) + r_0^{2m}}}.\end{aligned} \tag{A8}$$

The Gouy phase is the difference in phase between $E(r,\varphi,z)$ and a plane wave measured/calculated along the optical axis

(i.e., at $r = 0$). Then, considering Eq. (A6) and the definition of Gouy phase, we need to calculate

$$\Phi_G = -i\mathrm{Log}\left(e^{-izk}\lim_{r\to 0} F(r,\varphi,z)\right). \tag{A9}$$

Taking the limit hugely simplifies the expression

$$\lim_{r\to 0} F(r,\varphi,z) = -e^{-i\Phi(z)}e^{izk} = e^{-i\Phi(z)}e^{izk}e^{i\pi}, \tag{A10}$$

which means that

$$\begin{aligned}\Phi_G &= -i\mathrm{Log}\left(e^{-izk}e^{-i\Phi(z)}e^{izk}e^{i\pi}\right)\\ &= -\Phi(z)+\pi = -\arctan(z/z_0)+\pi. \end{aligned}\tag{A11}$$

The above coincides with the Gaussian case (up to an overall phase of π). In this work, however, we kept the usual style of presenting the Gouy phase ($\Phi(z)$) as increasing from $-\pi/2$ toward the beam focus and further to $\pi/2$.

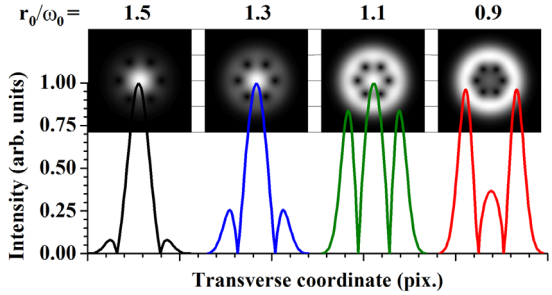

Fig. 11. Power density distributions (upper row) and transverse intensity profiles (graphs) of coaxial superpositions of Laguerre–Gaussian vortex beams and a Gaussian beam for six OVs ($m = 6$) and for different necklace-ring-radius-to-Gaussian-beam-width ratios r_0/ω_0. For all these substantially different intensity distributions, the analytical results show that from the beam waist to "infinity," the Gouy phase evolves according to the dependence $\Phi = \arctan(z/L_D)$. This was numerically confirmed.

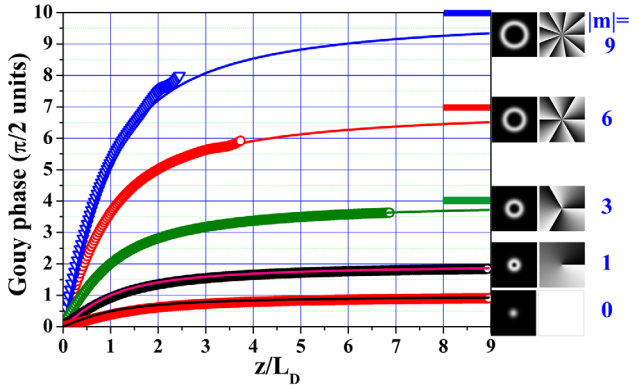

Fig. 12. Numerical results. Gouy phases for Laguerre–Gaussian beams with azimuthal mode indices $|m| = 0$, 1, 3, 6, and 9 and with radial mode index $p = 0$. Grayscale panels to the right: Initial amplitude (left column) and phase distributions (right; black and white—0 and 2π) of the respective LG modes. The colored bars to the right mark the asymptotic values of the Gouy phases when they are not reached in the simulations due to indications of the onset of computational error accumulation.

APPENDIX B

In Fig. 11 are shown more examples of coaxial superpositions of six Laguerre–Gaussian vortex beams and a Gaussian beam for different necklace-ring-radius-to-Gaussian-beam-width ratios. Numerically calculated Gouy phases of Laguerre–Gaussian beams with zero radial mode index and with varying azimuthal mode indices compared to the analytical results are shown in Fig. 12.

Funding. Bulgarian Science Fund (КП-06-Н78/6); Ministry of Education and Science (DO-102/26.06.2025, BG16RFPR002-1.014-0006, BG-RRP-2.004-0008-C01).

Acknowledgment. We acknowledge funding of the Bulgarian National Science Fund (project КП-06-Н78/6). The work was also supported by the Bulgarian Ministry of Education and Science as a part of the National Roadmap for Research Infrastructure, project ELI ERIC BG (project DO1-102/26.06.2025), and by the European Regional Development Fund under "Research Innovation and Digitization for Smart Transformation" program 2021-2027 under the Project BG16RFPR002-1.014-0006 "National Centre of Excellence Mechatronics and Clean Technologies." N.G., M.M., L.S., and A.D. were also supported by the European Union NextGenerationEU through the "National Recovery and Resilience Plan of the Republic of Bulgaria, project BG-RRP-2.004-0008-C01."

Disclosures. The authors declare no conflicts of interest.

Data availability. Data underlying the results presented in this paper are not publicly available at this time but may be obtained from the authors upon reasonable request.

REFERENCES

1. E. H. Linfoot and E. Wolf, "Phase distribution near focus in an aberration-free diffraction image," Proc. Phys. Soc. B **69**, 823 (1956).
2. G. W. Farnell, "Measured phase distribution in the image space of a microwave lens," Can. J. Phys. **36**, 935–943 (1958).
3. W. H. Carter, "Anomalies in the field of a Gaussian beam near focus," Opt. Commun. **7**, 211–218 (1973).
4. Y. Toda, S. Honda, and R. Morita, "Dynamics of a paired optical vortex generated by second-harmonic generation," Opt. Express **18**, 17796–17804 (2010).
5. X. Wang, W. Sun, Y. Cui, *et al.*, "Complete presentation of the Gouy phase shift with the THz digital holography," Opt. Express **21**, 2337–2346 (2013).
6. M. Liebmann, A. Treffer, M. Bock, *et al.*, "Spectral anomalies and Gouy rotation around the singularity of ultrashort vortex pulses," Opt. Express **25**, 26076–26088 (2017).
7. X. Pang and T. D. Visser, "Manifestation of the Gouy phase in strongly focused, radially polarized beams," Opt. Express **21**, 8331–8341 (2013).
8. L. Stoyanov, A. Stefanov, A. Dreischuh, *et al.*, "Gouy phase of Bessel-Gaussian beams: theory vs. experiment," Opt. Express **31**, 13683–13699 (2023).
9. S. Feng and H. G. Winful, "Physical origin of the Gouy phase shift," Opt. Lett. **26**, 485–487 (2001).
10. N. Gorunski, M. Mincheva, E. Lazarov, *et al.*, "Tuning the Gouy phase of laser beams by necklace-like structures of optical vortices," Proc. Bulg. Acad. Sci. **78**, 975–982 (2025).
11. J. Hamazaki, Y. Mineta, K. Oka, *et al.*, "Direct observation of Gouy phase shift in a propagating optical vortex," Opt. Express **14**, 8382–8392 (2006).
12. J. He, X. Wang, D. Hu, *et al.*, "Generation and evolution of the terahertz vortex beam," Opt. Express **21**, 20230–20239 (2013).
13. J. F. Nye and M. V. Berry, "Dislocations in wave trains," Proc. R. Soc. London A **336**, 165–190 (1974).
14. A. S. Desyatnikov, Y. S. Kivshar, and L. Torner, "Chapter 5: Optical vortices and vortex solitons," in *Progress in Optics* (Elsevier, 2005), pp. 291–391.
15. L. Stoyanov, S. Topuzoski, G. G. Paulus, *et al.*, "Optical vortices in brief: introduction for experimentalists," Eur. Phys. J. Plus **138**, 702 (2023).

16. N. R. Heckenberg, R. McDuff, C. P. Smith, *et al.*, "Generation of optical phase singularities by computer-generated holograms," Opt. Lett. **17**, 221–223 (1992).
17. L. Stoyanov, N. Gorunski, M. Zhekova, *et al.*, "Vortex interactions revisited: formation of stable elementary cells for creation of rigid vortex lattices," Proc. SPIE **11047**, 110471D (2019).
18. K. K. Tripathi, G. Sinha, A. Dixit, *et al.*, "Generation of cylindrical-vector beams using a dual slow-axis liquid crystal spatial light modulator," IEEE Photonics Technol. Lett. **38**, 539–542 (2026).
19. Laxminarayan, K. K. Tripathi, P. Kumar, *et al.*, "Single-phase modulated optical skyrmions for information security applications," Opt. Express **33**, 51116–51141 (2025).
20. L. Allen, M. W. Beijersbergen, R. J. C. Spreeuw, *et al.*, "Orbital angular momentum of light and the transformation of Laguerre-Gaussian laser modes," Phys. Rev. A **45**, 8185–8189 (1992).
21. P. Polesana, M. Franco, A. Couairon, *et al.*, "Filamentation in Kerr media from pulsed Bessel beams," Phys. Rev. A **77**, 043814 (2008).
22. R. W. Boyd, *Nonlinear Optics*, 3rd ed. (Academic, 2008).
23. R. F. Offer, A. Daffurn, E. Riis, *et al.*, "Gouy phase-matched angular and radial mode conversion in four-wave mixing," Phys. Rev. A **103**, L021502 (2021).
24. F. Lindner, G. G. Paulus, H. Walther, *et al.*, "Gouy phase shift for few-cycle laser pulses," Phys. Rev. Lett. **92**, 113001 (2004).
25. B. Ghomashi, R. Reiff, and A. Becker, "Coherence in macroscopic high harmonic generation for spatial focal phase distributions of monochromatic and broadband Gaussian laser pulses," Opt. Express **29**, 40146–40160 (2021).
26. A. A. Kovalev, V. V. Kotlyar, and A. G. Nalimov, "Topological charge and asymptotic phase invariants of vortex laser beams," Photonics **8**, 445 (2021).
27. P. Munjal and K. P. Singh, "A single-lens universal interferometer: towards a class of frugal optical devices," Appl. Phys. Lett. **115**, 111102 (2019).
28. J. Peatross and M. V. Pack, "Visual introduction to Gaussian beams using a single lens as an interferometer," Am. J. Phys. **69**, 1169–1172 (2001).
29. L. Stoyanov, G. Maleshkov, M. Zhekova, *et al.*, "Far-field pattern formation by manipulating the topological charges of square-shaped optical vortex lattices," J. Opt. Soc. Am. B **35**, 402–409 (2018).
30. D. Neshev, A. Dreischuh, M. Assa, *et al.*, "Motion control of ensembles of ordered optical vortices generated on finite extent background," Opt. Commun. **151**, 413–421 (1998).